Efficient Electrocatalysts for Alkaline Oxygen Evolution Reaction from Wolframite Derived Heteroatom Materials

Linghui Li, Sandrine Tusseau-Nenez, Clément Marchat, Cédric Tard

Efficient Electrocatalysts for Alkaline Oxygen Evolution Reaction from Wolframite Derived Heteroatom Materials

Linghui Li,[a] Sandrine Tusseau-Nenez,[b] Clément Marchat,[b] and Cédric Tard*[a]

[a] L. Li, C. Tard - Laboratoire de Chimie Moléculaire (LCM), CNRS École Polytechnique, Institut Polytechnique de Paris, 91120 Palaiseau, France E-mail: cedric.tard@polytechnique.edu

[b] S. Tusseau-Nenez, C. Marchat - Laboratoire de Physique de la Matière Condensée (PMC), CNRS École Polytechnique, Institut Polytechnique de Paris, 91120 Palaiseau, France

New materials for oxygen evolution reaction (OER) electro- Mn, Ni, Co) towards OER in basic conditions. Our results showed catalysts in alkaline conditions have been highly investigated in that $Ni_{0.5}Mn_{0.5}WO_4$ is a promising electrocatalyst, exhibiting ease recent years for the advancement of water splitting. However, of preparation, stability over the course of our experiments, and questions such as the lack of stability and the use of noble OER activity comparable to the standard iridium oxide. This metals as electrocatalysts still need to be addressed. In this study highlights the potential of wolframite tungsten-based study, we report the synthesis and electrocatalytic properties of materials as a new class of electrocatalysts for OER in alkaline a series of wolframite tungsten-based materials (MWO_4, M=Fe, conditions.

1. Introduction

As is widely recognized, the growing of the economy and of the population over the past decades make it increasingly imperative to develop renewable energy sources as alternatives to fossil fuels.[1,2] Nonetheless, several problems arose with the intense use of these energy sources and their sporadic and unreliable nature, due to the intermittency of the sun irradiation and wind power. On the other hand, utilizing renewable energy sources for water splitting allows to store electrical energy within chemical bonds. Major advances have been brought in the field of hydrogen and oxygen evolution recently, but with still some issues regarding the nature of the electrocatalysts.[3] Water electrolyzer technologies represent an ideal path to generate clean hydrogen from renewable energy sources. However, one of the challenges relies in the fact that highly efficient and stable electrocatalysts typically involve noble metals, such as platinum and iridium.[4] Three main electrochemical technologies for water splitting have emerged: the conventional alkaline electrolysis technology, while well-established and developed for several decades, exhibits a relatively slow response to changes in power supply;[5,6] proton exchange membrane (PEM) technology demonstrates excellent efficiency and stability, but relies currently solely on noble metals electrocatalysts;[7,8] the anion exchange membrane (AEM) technology offers the advantage of employing cheap and abundant transition metals as electrocatalysts for both oxygen evolution reaction (OER) and hydrogen evolution reaction (HER), while maintaining performance to a significant degree.[9,10] As such, AEM aims to combine the advantages of alkaline and PEM electrolyzers, while the nature and the stability of the membrane within the device remains a challenge to be addressed.[11,12]

Towards the development of AEM technology, transition metal oxides have been employed as alternative electrocatalysts to adjust their properties in order to enhance OER performance. In particular, tungsten-based electrocatalysts have raised increasing attention due to their abundance, high stability, and distinctive electronic structures.[13,14] Among the different tungsten ores available, wolframite (MWO_4, M=Fe, Mn, Ni, Zn, Cu, Co) represents the most prevalent source of this element worldwide.[15,16] Various methods can be employed for preparing synthetic forms of wolframites, including hydrothermal method, solvothermal method, sonochemical synthesis, and microwave technique.[17,18] In general, all of the chemical synthesis methods mentioned are facile. For instance, MWO_4 (M=Co, Cu, Mn, Zn) was successfully synthesized using a one-pot solvothermal method, where the control of synthesis condition can be easily set up[19] while $Cu_{1-x}Ni_xWO_4$ could be prepared through a straightforward sonochemical method, which is a versatile technique for the preparation of complex structures with different morphologies.[20] Furthermore, reports suggested that derivative-wolframite materials can be considered as excellent functional materials due to their unique electronic structures, and the presence of different transition metals within its structure can lead to synergistic effects in the OER reaction and other applications.[21–23] Adib et. al synthesized $CoWO_4$ nanoparticles through a chemical precipitation reaction and

observed remarkable performances in supercapacitors.[24] $Ni_xMn_{1-x}WO_4$ derivatives deposited on nickel foam (NF) were successfully synthesized, and the $Ni_{0.90}Mn_{0.10}WO_4$/NF electrode exhibited higher conductivity and supercapacitor properties.[25] While there have been numerous reports investigating photocatalytic and supercapacitor properties, fewer studies related to electrochemical water splitting by wolframite materials have been reported.[19] Brijesh et al. reported that a combination of $ZnWO_4$ and polypyrrole can enhance the bifunctional electrocatalyst HER/OER properties for water splitting.[26] Kumar et al. investigated carbon nanofibers (CNF) doped with derivatives of MWO_4 (M=Mn, Co, Ni, Mn Co, Mn Ni, Ni Co) to build nanostructured electrodes, and among these different materials $MnNiWO_4$/CNF exhibited superior photoelectrochemical performance for water splitting in basic conditions, reaching under irradiation an activity of 53 mA·cm ^{2} at 1.6 V (vs Ag/AgCl).[27]

To further explore the potential of tungsten oxide derivatives for the OER, we present here a novel approach to enhancing the potential of materials based on natural wolframite ($Fe_xMn_{1-x}WO_4$). This method allowed exploring the effect of isotropic substitution of iron and manganese cations which significantly influences their electrocatalytic properties. We successfully synthesized $Fe_{0.5}Mn_{0.5}WO_4$, $Ni_{0.5}Mn_{0.5}WO_4$, $Fe_{0.5}Ni_{0.5}WO_4$, $Fe_{0.5}Co_{0.5}WO_4$, and $Co_{0.5}Mn_{0.5}WO_4$ via a hydrothermal reaction, and characterized by X-ray diffraction analysis (XRD) and scanning electron microscope (SEM). Among the synthesized materials, $Ni_{0.5}Mn_{0.5}WO_4$ exhibited superior electrocatalytic activity under alkaline conditions (0.1 M KOH), comparable to IrO_2, the standard reference sample for OER.[28,29] The use of natural wolframite as a base material is not only innovative but also advantageous due to its wide availability and cost-effectiveness. This suggests that $Ni_{0.5}Mn_{0.5}WO_4$ could be a more efficient and economical alternative to IrO_2 for OER applications. Furthermore, the preparation of solid solutions of $Ni_xMn_{1-x}WO_4$ (x=1, 0.9, 0.75, 0.6, 0.5, 0.4, 0.25, 0) allows for a comprehensive investigation into the influence of the composition on the electrocatalytic activity, with an optimal equimolar Ni:Mn ratio for the highest performances.

Materials and Methods

Materials and Reagents

Reagents were all analytical-grade and purchased from Sigma Aldrich. Nafion®D-521 dispersion (5% w/w) was purchased from Alfa Aesar and Carbon Vulcan®XC72R was purchased from Cabot. All solutions were prepared with 18.2 mΩ·cm Millipore water. The $M1_xM2_{(1-x)}WO_4$ (M1/2=Fe, Mn, Ni, Co) materials were synthesized by a facile one-step hydrothermal method:[30] a 6 mM solution of $Na_2WO_4 \cdot 2H_2O$ (30 mL) was added dropwise to a 6 mM solution (30 mL) of $MnCl_2 \cdot 2H_2O$, $(NH_4)_2Fe(SO_4)_2 \cdot 6H_2O$, $Ni(CH_3COO)_2 \cdot 4H_2O$ or $Co(CH_3COO)_2 \cdot 4H_2O$. All reagents were purchased from Sigma Aldrich and were of analytical grade (99.8%). After 0.5 h of magnetic stirring, the solution was transferred to a 100 mL Teflon-lined autoclave, sealed, and maintained at 180°C for 24 h. Subsequently, the solution was allowed to cool to room temperature. The resulting products were filtered and washed three times with absolute ethanol and distilled water to eliminate impurities and unreacted materials. The samples were then dried overnight in an oven at 60°C, to obtain a yield of around 90%. For the synthesis wolframite, the transition metal salts were mixed in a 1:1 ratio, and then a solution of $Na_2WO_4 \cdot 2H_2O$ was added dropwise to the above mixed solution (Table 1).

Material Characterization Methods

X-ray diffraction (XRD) was carried out using an X-ray diffractometer (Bruker D8 Advance, Germany) in Bragg-Brentano geometry and equipped with the LynxEye XE T detector (1D mode and maximum detector opening), an automatic anti-scatter screen position and Cu radiation (Kα1=1.5406 Å and Kα2=1.5445 Å). The patterns were recorded at room temperature using 2.5°. Soller slits and a divergence slit of 0.5°, from 5 to 80° (2θ) range with a step size of 0.02° and a scan speed of 0.3 sec/step. Phase identification was performed with the PANalytical Highscore Plus software using the PDF2-release 2004 database. The crystallographic information files were downloaded from the Inorganic Crystal Structure Database (ICSD).

The Rietveld refinements were performed using the Maud software.[31] The Popa anisotropic size-strain model was used to take into account the anisotropy of the crystallite size and the microstrains.[32] When a second phase was identified, a simple anisotropic Delft model was chosen. Due to the tendency of platelets or nanorods to approach each other with parallel orientations, the XRD pattern exhibits a strong preferred orientation. The

arbitrary texture model (a Le Bail fit) was chosen even though it is not a real texture model. It is useful for refining peak positions only and allows the peak broadening to be described correctly. For all patterns, the refined parameters were the phase scale factor, sample displacement, background modelled by a 6term polynomial function, unit cell, microstructure, and temperature factor.

The micromorphology and chemical composition of samples were observed by coupled Scanning Electron Microscope (SEM) (Hitachi S-4800, Japan), using acceleration voltages of 15 kV and 30 kV along a mixed (top and side) secondary electron detection, and energy dispersive X-ray spectroscopy (EDX) (THERMO ultradry, USA). Transmission Electron Microscopy (TEM) measurement was done using a Titan ETEM 300 G2 (Thermo Fisher, USA).

Electrochemical Characterization

Three-Electrode Cell Experiments

All electrochemical characterizations were performed using a rotating disk electrode (RDE, Pine Research Instrumentation) with an Autolab PGSTAT 12 potentiostat (Metrohm). The three-electrode cell setup included Hg/HgO (ALS Co., Ltd, Japan) as a reference electrode (RE), graphite rod as the counter electrode (CE), and a 5-mm diameter glassy carbon carefully polished and rinsed in ethanol as a working electrode (WE) where the catalyst ink was deposited. The electrocatytic film was prepared using the following procedure: a solution containing 1 mg of the $M1_xM2_{(1-x)}WO_4$ electrocatalyst, 2 mg of carbon Vulcan in 250 µL of Nafion® and 250 µL of deionized water was sonicated in an ultrasonic bath for 20 minutes; then 8 µL of the solution was deposited on the working electrode and let dried in the air for 20 minutes at room temperature and then at 60°C for 30 minutes in an oven. To ensure the reliability of the experiment, three identical inks were prepared for each sample and triplicates were recorded for each ink. All experiments with the loaded WE were carried out at a constant rotating rate speed of 1600 rpm in a cell containing freshly prepared 0.1 M KOH solution (pH=13) as supporting electrolyte. The scan rate was 0.01 $V{\cdot}s^{-1}$, and the ohmic drop was carefully compensated for each measurement (ca. 30 Ω). All the results were compared to a commercial IrO_2 (Thermo Fisher, USA) for reference.

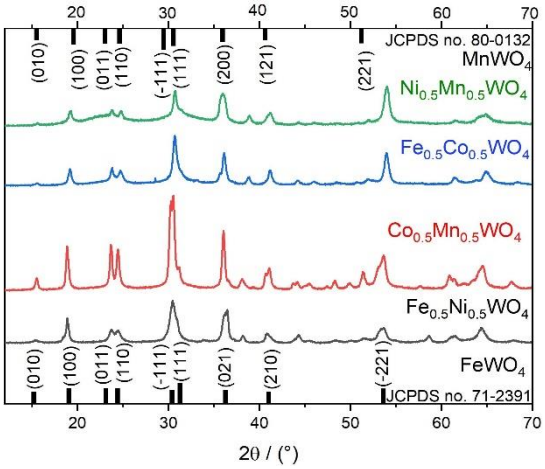

Figure 1. XRD patterns of the wolframite derivatives.

Table 1. Electrocatalysts synthesis.

Mixed ratio 1:1		W Source	Final Product
$(NH_4)_2Fe(SO_4)_2 \cdot 6H_2O$	$MnCl_2 \cdot 2H_2O$	$Na_2WO_4 \cdot 2H_2O$	$Fe_{0.5}Mn_{0.5}WO_4$
$Ni(CH_3COO)_2 \cdot 4H_2O$	$MnCl_2 \cdot 2H_2O$	$Na_2WO_4 \cdot 2H_2O$	$Ni_{0.5}Mn_{0.5}WO_4$
$(NH_4)_2Fe(SO_4)_2 \cdot 6H_2O$	$Ni(CH_3COO)_2$	$Na_2WO_4 \cdot 2H_2O$	$Fe_{0.5}Ni_{0.5}WO_4$
$(NH_4)_2Fe(SO_4)_2 \cdot 6H_2O$	$Co(CH_3COO)_2$	$Na_2WO_4 \cdot 2H_2O$	$Fe_{0.5}Co_{0.5}WO_4$
$Co(CH_3COO)_2 \cdot 4H_2O$	$MnCl_2 \cdot 2H_2O$	$Na_2WO_4 \cdot 2H_2O$	$Co_{0.5}Mn_{0.5}WO_4$

Electrolysis

To test the stability of the prepared materials, current-constant electrolyses were performed for six hours at 5 mA·cm^2, using similar experimental conditions as the OER water splitting threeelectrode cell tests mentioned above.

2. Results and Discussion

2.1. Study of $M1_xM2_{(1-x)}WO_4$ (M1/2=Fe, Mn, Ni, Co) Electrocatalysts for the OER

2.1.1. Synthesis and Characterization of MWO_4 (M=Fe, Mn, Ni, Co)

The XRD patterns of $M1_xM2_{(1-x)}WO_4$ (M1/2=Fe, Mn, Ni, Co) samples exhibit similar patterns, where the eight strongest characteristic diffraction peaks for the monoclinic wolframite (JCPDS no. 71–2391);[33] the peaks at 2θ=15.5°, 18.3°, 23.7°, 24.4°, 30.3°, 30.4°, 36.2°, 41.1°, and 53.4°, correspond to the (010), (100), (011), (110), (111), (111), (021), (210) and (221) crystal planes, respectively. (Figure 1).

Table 2 summarizes the refined crystallographic parameters and the Rietveld error indices on these powders. The reference patterns used from PDF2 database are 01–072-1189 for $NiWO_4$ and 01–080-0132 for $MnWO_4$, and the corresponding ICSD patterns are 15852 and 15850 respectively. No patterns are available in the crystallographic databases for our $M1_xM2_{(1-x)}WO_4$ compounds. As expected, as the atomic radius of the M ions increases, the unit cell volume increases. B. H. Toby[34] defined and discussed accurately the different error indices given in a Rietveld refinement. Our calculated values indicate that the crystallographic model (R_{Bragg}) and the refinement (σ, R_{wp}) are correct, compared with the published values available for nanocrystalline materials.[35–37]

Table 3 gives the microstructural information obtained from the Popa anisotropic size-strain model. From Maud analysis, the crystallite size (CS) corresponds to the diameter of the crystallite, and the microstrain is reported as $\langle\varepsilon^2\rangle^{1/2}$ described in the Popa model. All the samples have a nanorod-type crystalline shape, except for $Ni_{0.5}Mn_{0.5}WO_4$ where the shape is similar to platelets. The low values for the microstrains indicate that few structural defects are present in the nanopowders.

It is possible to compute the crystallinity of a sample from its diffractogram using the Degree of Crystallinity (DOC) method.[38] The results are given in Table 4. In each composition, a non-negligible contribution of amorphous phase is observed.

Table 2. The refined crystallographic parameters and Rietveld error indices of samples.

Sample	a (Å)	b (Å)	c (Å)	β (°)	V (Å^3)	σ	R_{wp} (%)	R_{Bragg} (%)
$Fe_{0.5}Ni_{0.5}WO_4$	4.606	5.647	4.943	90.1	128.6	1.96	6.96	5.41
$Co_{0.5}Mn_{0.5}WO_4$	4.748	5.778	5.012	89.3	137.5	2.17	7.79	6.07
$Fe_{0.5}Co_{0.5}WO_4$	4.654	5.679	4.963	89.9	131.5	1.79	7.60	5.66
$Ni_{0.5}Mn_{0.5}WO_4$	4.730	5.789	4.969	89.5	136.1	1.56	6.72	5.15

Table 3. Microstructural information (CS = crystallite size and MS = microstrain) obtained from the Popa anisotropic size-strain model, for the specific crystallographic orientations in the cell.

Sample	CS (Å)/100	MS (%) rms/100	CS (Å)/010	MS (%) rms/010	CS (Å)/002	MS (%) rms/002
$Fe_{0.5}Ni_{0.5}WO_4$	20	0.0027	11	0.0028	70	0.0075
$Co_{0.5}Mn_{0.5}WO_4$	30	0.0061	16.5	0.0009	70	0.0021
$Fe_{0.5}Co_{0.5}WO_4$	31	0.0033	31	0.0040	21	0.0002
$Ni_{0.5}Mn_{0.5}WO_4$	24	0.0006	111	0.0168	67	0.0053

rms: root mean square, "/hkl": in the hkl direction.

3.1.2 Electrochemical Performance Comparison of $M1_xM2_{(1-x)}WO_4$ for OER in Basic Conditions

The synthetized materials are showing disparate catalytic activities regarding OER. As outlined in Figure 2, to reach a current density of 10 mA·cm ^{2}, $Ni_{0.5}Mn_{0.5}WO_4$ outperformed IrO_2, with an overpotential of only 1.82 V vs RHE as opposed to 2.18 V for IrO_2 recorded in our experimental conditions. The series is then followed by $Fe_{0.5}Ni_{0.5}WO_4$,

$Fe_{0.5}Co_{0.5}WO_4$, and finally $Co_{0.5}Mn_{0.5}WO_4$, for which the overpotential recorded was much more modest, with values of 2.41 V, 2.48 V, and 2.70 V to deliver 10 mA·cm ^{2}, respectively. This remarkable electrocatalytic activity for the $Ni_{0.5}Mn_{0.5}WO_4$ material emphasized the possible synergetic effect of the heterometallic structure synthesized. This result aligns with a previous study by Karkera et al., in which an efficient bifunctional catalyst was designed to tune the electronic properties of cobalt–manganese tungstate derivatives, $Co_{1-x}Mn_xWO_4$ (x=0, 0.25, 0.5, 0.75, 1).[39] In their study, solid solutions were synthesized and investigated, revealing that replacing an optimum amount of Co with Mn can enhance the electrochemical catalytic activity towards the OER.

Table 4. Calculation the crystallinity of $M1_xM2_{(1-x)}WO_4$.

Sample	% of Amorphous Phase	% of Crystalline Phase
$FeCoWO_4$	18.4	81.6
$FeNiWO_4$	27.9	72.1
$NiMnWO_4$	22.2	77.8
$CoMnWO_4$	25.8	74.2

2.2. $Ni_XMn_{1-x}WO_4$ Electrocatalyst Derivatives for the OER

2.2.1. Structure and Chemical Composition Analysis

Based on XRD measurements (Figure 3), it can be evidenced that as the quantity of Mn^{2+} increases, the width of the XRD diffraction peak narrowed, indicating an increase of the crystallite size and a release of the microstrains.

A careful reading was necessary to perform correct Rietveld refinements. Indeed, in the angular window 34–37° 2θ, the 002 peak is shifted to the right as the amount of Mn^{2+} increases in the composition. A shoulder to the left of the peak is clearly observed for compositions between 40 and 60 mol% Mn^{2+}, and less visible but present for compositions with 25 and 75 mol% Mn^{2+}. In those cases, two phases were considered in the refinements: $NiWO_4$-type phase corresponding to the shoulder which is exactly at the position of the 002 Bragg peak for pure $NiWO_4$ (the two bumps at 22.4° and 31.5° for $NiWO_4$ are also observed) and a solid solution $Ni_xMn_{1-x}WO_4$. Moreover, when the quantity of Ni^{2+} increases, the intensity of the background noise increases (see Figures S1 and S2). A scattering signal under the diffraction peaks is observed, which may be the consequence of local disorders in the crystallographic structure

Table 5. Crystallinity calculation for $Ni_xMn_{1-x}WO_4$.

Mn^{2+} Content	% of Amorphous Phase	% of Crystalline Phase
0	70.2	29.8
0.1	63.4	36.6
0.25	61.5	38.5
0.4	41.4	58.6
0.5	35	65
0.6	29	71
0.75	17	83
1	9.3	90.7

Considering that the aim of this study is to define an optimum Ni/Mn ratio, further investigation would be needed to clarify the disorder in the microstructure of the nanopowders, so that a Rietveld refinement could be carried out for quantitative analysis of the phases and calculation of their chemical content.

As a consequence, a systematic Le Bail refinement was performed on each sample, focusing on the crystallographic structure (positions of the peaks are not affected by the presence of diffusion), and peak broadening of the crystalline phases. For compositions from 40 to 60% of Mn^{2+}, $NiWO_4$ phase was added and all the cell parameters were set to those calculated for the pure phase. All the results for the $Ni_xMn_{1-x}WO_4$ are summarized in Table 6.

For $NiWO_4$ and $Ni_{0.9}Mn_{0.1}WO_4$ samples, with similar diffractograms, the Rietveld refinement leads to a bigger cell volume comparing to the reference pattern (Vol=127.84 Å^3), even though a large error bar should be considered due to their low crystallinity. For $MnWO_4$, the Rietveld refinement leads to cell parameters very close to the reference (Vol=138.92 Å^3).

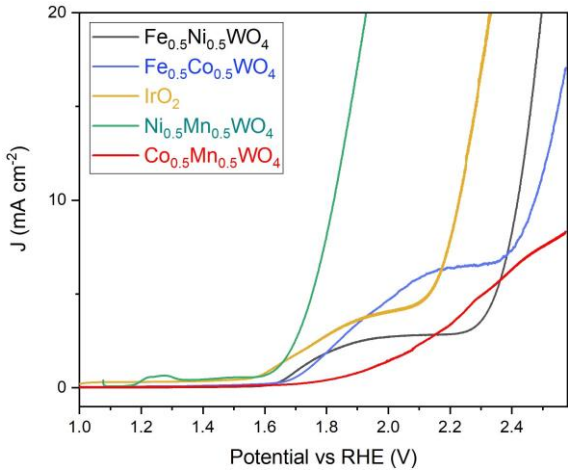

Figure 2. Linear sweep voltammetry (LSV) curves of samples recorded at 0.01 V·s ^{1} in a 0.1 M KOH solution (pH=13).

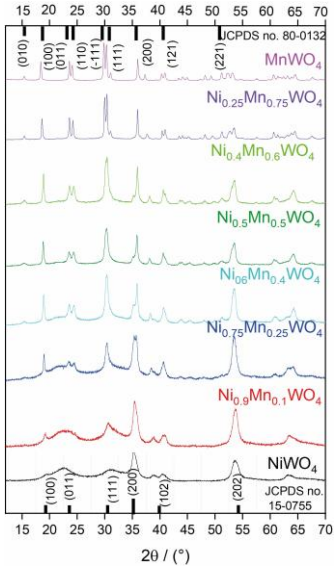

Figure 3. XRD patterns of the $Ni_XMn_{1-x}WO_4$ series.

Table 6. Cell parameters and apparent crystallite volumes calculated for the $Ni_xMn_{1-x}WO_4$ samples.

Composition	a (Å)	b (Å)	c (Å)	Beta (°)	Cell Volume (Å^3)
$NiWO_4$	4.126	5.680	5.828	93.2	136.37
$Ni_{0.9}Mn_{0.1}WO_4$	4.602	5.701	5.081	90.1	133.30
$Ni_{0.75}Mn_{0.25}WO_4$	4.656	5.831	5.063	89.9	137.46
$Ni_{0.6}Mn_{0.4}WO_4$	4.717	5.786	5.031	90.1	137.28
$Ni_{0.5}Mn_{0.5}WO_4$	4.752	5.811	5.051	89.5	139.45
$Ni_{0.4}Mn_{0.6}WO_4$	4.741	5.793	5.025	90.7	137.98
$Ni_{0.25}Mn_{0.75}WO_4$	4.783	5.778	5.009	89.0	138.40
$MnWO_4$	4.826	5.755	4.995	91.2	138.70

Crystallite sizes and microstrains are available from the Rietveld refinements and summarized in Table S1 for two main crystallographic directions, 0k0 where smallest crystallite sizes are calculated and hk0 for the biggest ones.

Anisotropy of shape is clearly evident. Pure compounds have nanorod-shape crystallites, while intermediate compositions have plateletshape crystallites. The samples with the highest Mn^{2+} content exhibit the lowest microstrain levels which can probably be associated with better crystallinity.

The chemical composition of the samples was determined using EDX. In each measurement, one to three regions were examined, and the Ni/Mn content was quantified using the PhiRho-Z model (Table S2). The measured Ni and Mn contents were consistent with the theoretical formula within the EDX experimental error (Figure S3).

2.2.2. Morphology Comparison

The morphology of the samples was examined through SEM (Figure 4). Regarding $NiWO_4$, we mostly observed spherical aggregates of size between 280 nm to 500 nm composed of small ovoid (nanorods) particles, 5 to 30 nm in size, slightly larger than the crystallite size estimated from the DRX analysis. For $Ni_{0.9}Mn_{0.1}WO_4$, the particles morphology and size do not change, but non-spherical aggregates can be evidenced. For $Ni_{0.75}Mn_{0.25}WO_4$, two shapes were observed: platelets with thickness of 10–20 nm and length around 50–130 nm, and nanorods with similar size to previous composition. The platelets are mostly seen in non-spherical aggregates. For $Ni_{0.5}Mn_{0.5}WO_4$, platelets are observed for the particles of size 10–20 nm in thickness and 30–100 nm in width, slightly smaller than $Ni_{0.75}Mn_{0.25}WO_4$. Only a few spherical aggregates can be seen, the remaining forming layered-platelets. The $Ni_{0.25}Mn_{0.75}WO_4$ display bigger platelets with significant variation in sizes (15–55 nm thickness and 50–700 nm width). For $MnWO_4$, hexagonal nanorods were observed with size ranging from 55 nm to 85 nm for length and 30 nm to 45 nm for width. For $NiWO_4$ and $MnWO_4$ non-mixed samples, nanorod structures were observed with $MnWO_4$ particles being bigger than $NiWO_4$ ones. For mixed composition ($Ni_XMn_{1-x}WO_4$), the particles structure takes a platelet form which was predominant at high mixing value (x> =0.25). The size of the platelets changes drastically depending of the mix ratio with the minimum size seen on the 50/50 sample. The SEM images evidenced that a high amount of Ni^{2+} increases the particles aggregation, with $NiWO_4$ composed mostly of spherical aggregates.

As the amount of Mn^{2+} in the composition increases, the cell volume increases, in agreement with atomic radii. An apparent crystallite volume (based on crystallite sizes calculated from directions 100, 010 and 002) was calculated, and its evolution as a function of Mn^{2+} content is in agreement with SEM observations.

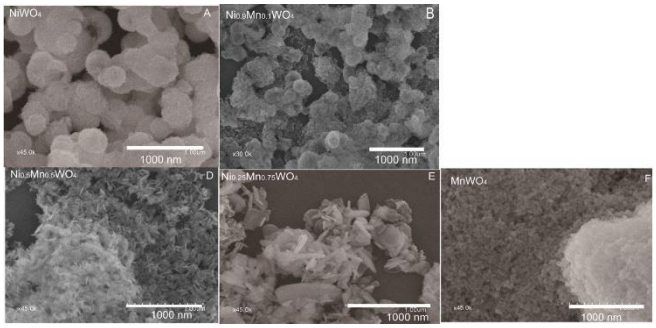

Figure 4. SEM images of $Ni_XMn_{1-x}WO_4$ (A) $NiWO_4$; (B) $Ni_{0.9}Mn_{0.1}WO_4$;(C) $Ni_{0.75}Mn_{0.25}WO_4$; (D) $Ni_{0.5}Mn_{0.5}WO_4$; (E) $Ni_{0.25}Mn_{0.75}WO_4$; (F) $MnWO_4$.

To further investigate the morphology of $Ni_{0.5}Mn_{0.5}WO_4$, TEM measurements were conducted. These images clearly revealed a mixture of two distinct shapes: the dark-shaded regions consisting mainly of nanorods with a length ranging from 70 nm to 100 nm, while the light-shaded regions primarily comprised platelets with varying degrees of aggregation (Figure 5).

2.2.3. Electrochemical Activity Comparison

The electrocatalytical activity of the various materials in the series was tested in a similar manner to the previous sets of materials as showed in Figure 6. Several non-catalytic redox events can be observed prior to the catalytic wave, corresponding to the oxidation of the transition metals within the materials. The exact attribution of those waves is not straightforward from LSV measurements and would certainly require further in-situ analysis in order to fully characterize those materials. The overpotential at 10 $mA{\cdot}cm^{-2}$ of $NiWO_4$, $Ni_{0.9}Mn_{0.1}WO_4$, $Ni_{0.75}Mn_{0.25}WO_4$,

$Ni_{0.6}Mn_{0.4}WO_4$, $Ni_{0.5}Mn_{0.5}WO_4$, $Ni_{0.4}Mn_{0.6}WO_4$, $Ni_{0.25}Mn_{0.75}WO_4$, and $MnWO_4$ were 2.68 V, 2.71 V, 2.87 V, 2.29 V, 1.83 V, 2.25 V, 2.76 V, 2.71 V, respectively. The observed trend suggests that an optimal composition can be achieved with a 1:1 Ni/Mn ratio (Figure 7), with a remarkable electrocatalytic comparable to iridium oxide under those experimental conditions. The series can be divided into three sets of electrocatalysts: poorly active (ca. η=2.7 V), moderately active (ca. η=2.2 V) and one highly active (ca. η=2.7 V) electrocatalysts. As for the most active material, $Ni_{0.5}Mn_{0.5}WO_4$, based on the XRD refinement, the fact that whatever the crystallinity of the sample or its tendency to stabilize two average compositions, the results are the same, showing that it is the nominal composition that seems to be the predominant parameter and not how the atoms organize themselves. The remaining materials in the series exhibited moderate to poor OER electrocatalytic activities, which validates the strategy for preparing the entire Ni/Mn series. The overpotentials and Tafel plots are compared in Table S3.

The excellent OER activity of $Ni_{0.5}Mn_{0.5}WO_4$ can be attributed to several factors. Firstly, the integrated platelets morphology with nanorods in $Ni_{0.5}Mn_{0.5}WO_4$ effectively increases the specific surface area and active sites, which improves electrochemical kinetics in the electrode/electrolyte region.[19,41] Secondly, the presence of oxygen vacancies due to the different ionic radii of Ni and Mn can further enhance the adsorption and desorption of OH ions. When nickel ions gradually replace the position of manganese ions in wolframite, the nickel oxygen octahedron and iron oxygen octahedron undergo different degrees of lattice distortion, leading to oxygen vacancies.[20,30] The appropriate concentration of oxygen vacancies can support the capability of adsorption and desorption of OH ions, thereby improving the OER activity of $Ni_{0.5}Mn_{0.5}WO_4$.

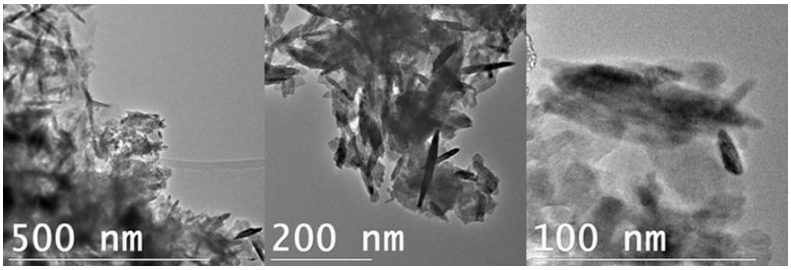

Figure 5. TEM images of $Ni_{0.5}Mn_{0.5}WO_4$.

To assess the stability of $Ni_{0.5}Mn_{0.5}WO_4$, a constant current of 5 mA·cm ^{2} was maintained for six hours, and the potential was monitored. The potential remained relatively stable along the experiment, with a slight improvement over time indicating the sustained electrochemical catalytic activity (Figure 8). Assessment of robustness within an AEM water electrolyzer still remains to be performed to measure the electrocatalytic activity over days/weeks of those materials.

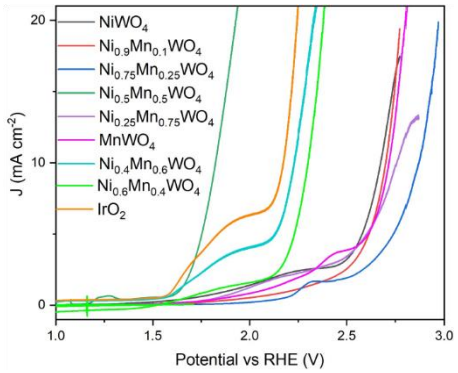

Figure 6. Linear sweep voltammetry (LSV) curves of $Ni_XMn_{1-x}WO_4$ recorded at 0.01 V·s ^{1} in a 0.1 M KOH solution (pH=13).

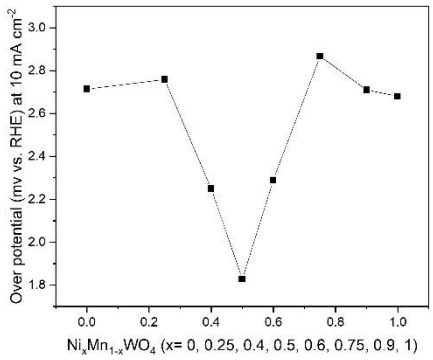

Figure 7. The changing trend of the overpotential at 10 mA·cm ^{2} with the increase of Ni content.

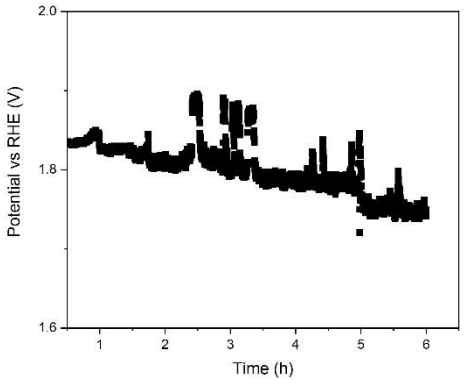

Figure 8. Galvanostatic test for 6 h@5 mA·cm ^{2}.

3. Conclusions

Developing a new class of transition-metal-based heterofunctional catalysts is a very promising way to electrocatalytically oxidize water into dioxygen. Among the different materials synthesized and characterized in this study, $Ni_{0.5}Mn_{0.5}WO_4$ demonstrated the highest performance in terms of activity, comparable with iridium oxide, and proved to be a stable catalyst within the time frame of the galvanostatic experiment. Further studies under AEM electrolyzer conditions will be conducted in the near future to assess the robustness of such materials for relevant durations.

Acknowledgements

This research was supported by 3rd Programme d'Investissements d'Avenir [ANR-18-EUR-0006-02] and by the private sponsor Fonds Ifker pour le Climat financed by Stéphane and Agnès Ifker. LL is acknowledging the China Scholarship Council (CSC).

Conflict of Interests

The authors declare no conflict of interest.

Data Availability Statement

The data that support the findings of this study are available in the supplementary material of this article.

References

[1] M. Ďurovič, J. Hnát, K. Bouzek, *J. Power Sources* **2021**, *493*, 229708.
[2] N. Mahmood, Y. Yao, J. W. Zhang, L. Pan, X. Zhang, J. J. Zou, *Adv. Sci.* **2018**, *5*, 1700464.
[3] A. Eftekhari, *Int. J. Hydrogen Energy* **2017**, *42*, 11053.

[4] A. J. Bard, L. R. Faulkner, H. S. White, *Electrochemical methods: fundamentals and applications*, John Wiley & Sons, **2022**, 838.
[5] T. B. Ferriday, P. H. Middleton, *Int. J. Hydrogen Energy* **2021**, *46*, 18489.
[6] G. McLean, T. Niet, S. Prince-Richard, N. Djilali, *Int. J. Hydrogen Energy* **2002**, *27*, 507.
[7] K. E. Ayers, E. B. Anderson, C. Capuano, B. Carter, L. Dalton, G. Hanlon, J. Manco, M. Niedzwiecki, *ECS Trans.* **2010**, *33*, 3.
[8] M. Carmo, D. L. Fritz, J. Mergel, D. Stolten, *Int. J. Hydrogen Energy* **2013**, *38*, 4901.
[9] S. Anantharaj, S. Noda, V. R. Jothi, S. Yi, M. Driess, P. W. Menezes, *Angew. Chem. Int. Ed.* **2021**, *60*, 18981.
[10] Y. Zheng, Y. Jiao, A. Vasileff, S. Z. Qiao, *Angew. Chem. Int. Ed.* **2018**, *57*, 7568.
[11] T.-W. Chen, P. Kalimuthu, G. Anushya, S.-M. Chen, V. Mariyappan, R. Ramachandran, *Materials* **2021**, *14*, 4420.
[12] F. Song, L. Bai, A. Moysiadou, S. Lee, C. Hu, L. Liardet, X. Hu, *J. Am. Chem. Soc.* **2018**, *140*, 7748.
[13] I. Roger, M. A. Shipman, M. D. Symes, *Nat. Chem. Rev.* **2017**, *1*, 0003.
[14] Z. P. Wu, X. F. Lu, S. Q. Zang, X. W. Lou, *Adv. Funct. Mater.* **2020**, *30*, 1910274.
[15] S. Thongtem, S. Wannapop, T. Thongtem, *T. Nonferr. Metal Soc.* **2009**, *19*, 100.
[16] L. Zhang, C. Lu, Y. Wang, Y. Cheng, *Mater. Chem. Phys.* **2007**, *103*, 433.
[17] M. Nakayama, A. Takeda, H. Maruyama, V. Kumbhar, O. Crosnier, *Electrochem. Commun.* **2020**, *120*, 106834.
[18] P. Siriwong, T. Thongtem, A. Phuruangrat, S. Thongtem, *CrystEngComm* **2011**, *13*, 1564.
[19] B. J. Rani, G. Ravi, S. Ravichandran, V. Ganesh, F. Ameen, A. Al-Sabri, R. Yuvakkumar, *Appl. Nanosci.* **2018**, *8*, 1241.
[20] R. K. Selvan, A. Gedanken, *Nanotechnology* **2009**, *20*, 105602.
[21] S. M. Alshehri, J. Ahmed, T. Ahamad, N. Alhokbany, P. Arunachalam, A. M. Al-Mayouf, T. Ahmad, *J. Sol-Gel Sci. Technol.* **2018**, *87*, 137. [22] X.-X. Wang, Y. Li, M.-C. Liu, L.-B. Kong, *Ionics* **2018**, *24*, 363.
[23] S. H. Yu, B. Liu, M. S. Mo, J. H. Huang, X. M. Liu, Y. T. Qian, *Adv. Funct. Mater.* **2003**, *13*, 639.
[24] K. Adib, M. Rahimi-Nasrabadi, Z. Rezvani, S. M. Pourmortazavi, F. Ahmadi, H. R. Naderi, M. R. Ganjali, *J. Mater. Sci. Mater. Electron.* **2016**, *27*, 4541.
[25] Z. Xia, Y. Huang, Y. Guo, Y. Wang, Z. Li, *J. Alloys Compd.* **2023**, *934*, 167977.
[26] K. Brijesh, K. Bindu, D. Shanbhag, H. Nagaraja, *Int. J. Hydrogen Energy* **2019**, *44*, 757.
[27] A. S. Kumar, R. R. Nallapureddy, M. R. Pallavolu, J. Nallapureddy, K. N. Sathya Sai, J. S. Kim, S. W. Joo, *Energy Fuels* **2022**, *36*, 15244.
[28] Z. Ma, Y. Zhang, S. Liu, W. Xu, L. Wu, Y.-C. Hsieh, P. Liu, Y. Zhu, K. Sasaki, J. N. Renner, *J. Electroanal. Chem.* **2018**, *819*, 296.
[29] C. Van Pham, M. Bühler, J. Knöppel, M. Bierling, D. Seeberger, D. Escalera-López, K. J. Mayrhofer, S. Cherevko, S. Thiele, *Appl. Catal. B* **2020**, *269*, 118762.
[30] L. Li, Y. Li, Y. Li, H. Ye, A. Lu, H. Ding, C. Wang, Q. Zhou, J. Shi, X. Ji, *Chem. Geol.* **2021**, *575*, 120253.
[31] L. Lutterotti, *Nucl. Instrum. Methods Phys. Res. Sect. B* **2010**, *268*, 334.
[32] N. Popa, *J. Appl. Crystallogr.* **1998**, *31*, 176.
[33] F. Yu, L. Cao, J. Huang, J. Wu, *Ceram. Int.* **2013**, *39*, 4133.
[34] B. H. Toby, *Powder Diffr.* **2006**, *21*, 67.
[35] V. Kumar, S. Kumari, P. Kumar, M. Kar, L. Kumar, *Adv. Mater. Lett.* **2015**, *6*, 139.
[36] A. Serafini, L. Lutterotti, S. Gross, S. Gialanella, *Powder Diffr.* **2017**, *32*, 63.
[37] K. Maniammal, G. Madhu, V. Biju, *Physica E* **2017**, *85*, 214.
[38] I. C. Madsen, N. V. Y. Scarlett, A. Kern, *Z. Kristallogr.* **2011**, *226*, 944.
[39] G. Karkera, T. Sarkar, M. D. Bharadwaj, A. S. Prakash, *ChemCatChem* **2017**, *9*, 3681.
[40] C. F. Holder, R. E. Schaak, *ACS Nano* **2019**, *13*, 7359. [41] C. Ling, L. Q. Zhou, H. Jia, *RSC Adv.* **2014**, *4*, 24692.